Cover Feature: Spectroscopic Characterisation of a Bio-Inspired Ni-Based Proton Reduction Catalyst Bearing a Pentadentate N 2 S 3 Ligand with Improved Photocatalytic Activity

Philipp Gotico, Dooshaye Moonshiram, Cunming Liu, Xiaoyi Zhang, Régis Guillot, Annamaria Quaranta, Zakaria Halime, Winfried Leibl, Ally Aukauloo

Spectroscopic Characterization of Bio-inspired Ni-based Proton Reduction Catalyst Bearing Pentadentate N_2S_3 Ligand with Improved Photocatalytic Activity

Philipp Gotico,[a] Dooshaye Moonshiram,*[b] Cunming Liu,[c] Xiaoyi Zhang,[c] Régis Guillot,[d] Annamaria Quaranta,[a] Zakaria Halime,[d] Winfried Leibl,[a] Ally Aukauloo*[a,d]

Abstract: Inspired by the sulphur-rich environment found in active hydrogenase enzymes, a novel Ni-based proton reduction catalyst with pentadentate N_2S_3 ligand was synthesized. When coupled with a $[Ru(bpy)_3]^{2+}$ photosensitiser and ascorbate as electron donor in a 1:1 mixture of dimethylacetamide and aqueous ascorbic acid/ascorbate buffer, the catalyst showed improved photocatalytic activity compared to a homologous counterpart with a tetradentate N_2S_2 ligand. The mechanistic pathway of photo-induced hydrogen evolution was comprehensively analysed through optical transient absorption (OTA) and time-resolved X-ray absorption spectroscopy (tr-XAS) revealing important electronic and structural changes in the catalytic system during photo-irradiation. It was found that the Ni (II) catalyst undergoes a photo-induced metal-centred reduction to form a Ni (I) intermediate bearing a distorted square bipyramidal geometry. Further kinetic analyses pointed out differences in charge separation dynamics between the pentadentate and tetradentate homologues.

Introduction

The crucial need to decarbonise the current energy mix that is heavily reliant on fossil fuels in view of the concomitant acceleration of global warming effect has urged the scientific community to find sustainable and clean ways to store and distribute energy. Relevant to this goal is the prospect of using hydrogen as a carbon-free fuel. Among the several issues to set-up a hydrogen-based economy, its sustainable production still holds the most attention.

One interesting approach for the progress of earth-abundant hydrogen-evolving catalysts lies in the development of bio-mimetic and bio-inspired catalysts with comparable stabilities and efficiencies to that of [Fe] and [NiFe] hydrogenases.[1–4] A typical characteristic of these enzymes' active sites is the sulphur-rich environment around the metal centres.[5] Functional models of metal-sulphur enzymes have been pioneered by the group of Sellmann[6–8] leveraging the unique electronic flexibility of sulphur ligands (such as sulphides, thiolates, and thioethers) which can accommodate both hard and soft ancillary ligands. Synthetic analogues of the [NiFe] hydrogenase have been well-reviewed by Lubitz,[2] Artero,[3] Pickett,[9] and Bouwman[10] showing various macrocyclic and acyclic nickel complexes with sulphur ligands coupled with oxygen, phosphorus, and nitrogen-containing structures. While most of these complexes have been studied for fundamental structural-functional understanding of hydrogenases, some possess stoichiometric and electrocatalytic proton reduction activity.[11–15]

Over the course of the past decade, there has been a significant incentive to photo-drive H_2 production by coupling a photoactive module with molecular electrocatalysts. Impressive photocatalytic activity of a NiN_2P_2-type Dubois' electrocatalyst[12] when associated with Ru or Eosin Y type photosensitiser (PS) and ascorbate as electron donor (ED) were for instance reported by Eisenberg, Holland and co-workers.[16] A fully coordinated nickel pyridinethiolate and pyrimidinethiolate catalyst of the type $Ni\text{-}N_3S_3$ with fluorescein as the PS and triethylamine as the ED was further characterised whereby one of the N atoms was suggested to be hemilabile and its protonated form was implied in the H-H bond formation.[17,18] This role was attributed to an S atom in the photocatalytically active nickel complexes with bidentate dithiolenes ($Ni\text{-}S_4$ type) reported by the group of Fan.[19] More recently, the group of Kojima demonstrated Ni complexes bearing thioethers in the form of tetradentate N_2S_2 ligands to show photocatalytic activity towards proton-reduction when coupled with a Ru PS.[20] Electrocatalytic and photocatalytic experiments in combination with DFT analysis favoured a scenario where cleavage of the Ni-H bond in the key reactive Ni^{II}-H intermediate constituted the rate limiting step of the catalytic reaction.

We report herein a comparative study on the light-driven catalytic activities of $\mathbf{Ni^{II}}$ complexes bearing an N_2S_3 and an N_2S_2 coordinating motif as illustrated in Scheme 1. Motivation for this work stems from the recent findings with sulphur-containing ligands and from the sulphur-rich environment found in active enzymes. We built on a previous study by Lucas and *coll.* where the authors showed, for a series of $\mathbf{Ni^{II}}$ complexes holding N_2S_x ligands, that an increase in the number of thioether functions in the coordination sphere causes an anodic shift in the potential of $\mathbf{Ni^{II/I}}$.[21] This study further expands upon the use of acyclic ligands which were shown to promote better stabilization of lower oxidation states compared to their macrocyclic counterparts.[21]

[a] Dr. P. Gotico, Dr. A. Quaranta, Dr. W. Leibl, Prof. A. Aukauloo
Institut de Biologie Integrative de la Cellule (I2BC),
Institut des Sciences du Vivant Frédéric-Joliot, CEA Saclay
91191 Gif-sur-Yvette, France
E-mail: ally.aukauloo@u-psud.fr
[b] Dr. D. Moonshiram
IMDEA Nanocience Institute,
Calle Faraday 9, Madrid 28760, Spain,
Email: dooshaye.moonshiram@imdea.org
[c] Dr. C. Liu, Dr. X. Zhang,
X-ray Science Division, Argonne National Laboratory,
9700 S. Cass Avenue, Lemont, IL, 60439, U.S.A
[d] Dr. R. Guillot, Dr. Z. Halime, Prof. A; Aukauloo
Institut de Chimie Moléculaire et des Matériaux d'Orsay (ICMMO)
UMR 8182 CNRS, Université Paris Sud
91405 Orsay, France

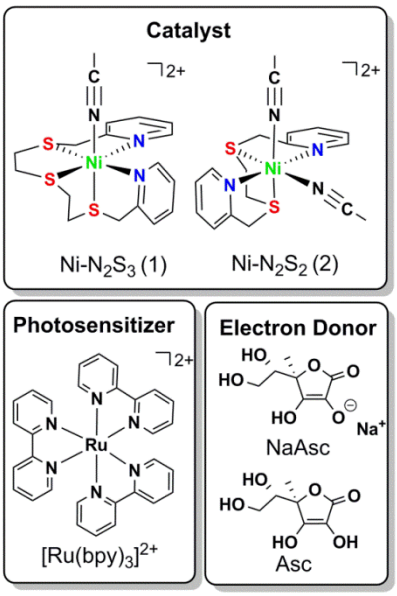

Scheme 1. Photocatalytic system consisting of Ni catalysts bearing N_2S_3 and N_2S_2 ligands, Ru photosensitiser and a mixture of sodium ascorbate and ascorbic acid as buffer and electron donor.

We envision that a systematic investigation on the N_2S_3 and N_2S_2 ligands would provide new insights for the current quest to shift the reduction potentials of the metal complexes towards more anodic values while maintaining an efficient catalytic pattern for proton reduction. Furthermore, coupling molecular catalysts with a photosensitiser to perform the light-induced H_2 formation still necessitates more in-depth investigation to unravel the limiting steps in the photocatalytic process.

Indeed, while most of the reported studies have comprehensively used electrochemical, spectroscopic, theoretical, and emission quenching experiments to propose a photocatalytic pathway, currently there is still a lack of mechanistic understanding of the photo-induced electron transfer events under catalytic conditions. Henceforth, capturing the spectral features of the reduced species of the catalyst and understanding the rate-determining step under light irradiation are crucial to comprehend the photocatalytic routes. We hereby couple our photocatalytic studies with time-resolved UV-Visible and X-ray absorption spectroscopies in order to mechanistically understand the activities of the investigated catalysts. The first photo-induced electron transfer from the photosensitiser to the catalysts was monitored by optical transient absorption (OTA) and time-resolved X-ray absorption spectroscopy (tr-XAS). Our results clearly evidenced the formation of a photo-induced reduced Ni^{I} species. Our analyses help to provide essential insights in the geometrical arrangements of the tetradentate N_2S_2 and pentadentate N_2S_3 nickel-based catalysts upon photo-reduction. Thus we start by reporting the synthesis, X-ray diffraction studies, and the electronic and structural characterization through X-ray absorption near edge structure (XANES) and extended X-ray absorption fine structure (EXAFS) analysis of the two Ni-based complexes bearing N_2S_2 and N_2S_3 ligands (Scheme 1). We then continue with a description of their electrochemical properties and their photo-induced activities when coupled with the Ru photosensitiser and ascorbate electron donor. The kinetic analysis, as well as the optical and electronic signature of the photo-reduced Ni^{I} species in complex **1** are finally described with a proposed mechanistic pathway for the photocatalytic cycle.

Results and Discussion

Synthesis, Crystal Structures and Electronic & Structural Characterizations through XANES, EXAFS, and TD-DFT

The pentadentate N_2S_3 ligand and tetradentate N_2S_2 ligand were synthesised following reported methods[21,22] as described in detail in the Experimental Section. Nickel (II) complexes **1** (Ni-N_2S_3) and **2** (Ni-N_2S_2) were obtained in good yields by complexation of the ligands with a Ni (II) perchlorate salt in methanol and were characterised accordingly (see Supplementary Information).

Single crystals suitable for X-ray diffraction analysis were obtained by slow diffusion of ethyl acetate in an acetonitrile (ACN) solution of the complex. X-ray structures of complexes **1** and **2** show a hexacoordinated Ni in a slightly distorted octahedral geometry (Figure 1). In both cases, the central metal is coordinated by two aromatic nitrogen atoms from the pyridines and three or two sulphur atoms from the thioethers. The first coordination sphere is completed by one (for **1**), or two (for **2**) nitrogen from acetonitrile solvent. The bond angles in catalyst **1** are more deviated from the ideal 90° compared to catalyst **2**, indicating a greater distortion of the coordination sphere in **1** (Table 1).

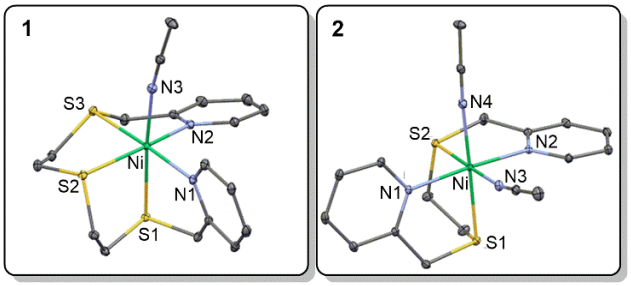

Figure 1. X-ray crystal structures (ORTEP thermal ellipsoids set at 30% probability) of catalysts **1** and **2**. Hydrogen atoms and counter anions are omitted for clarity.

Table 1. Selected bond lengths and angles of the X-ray crystal structures. All esds are estimated using the full covariance matrix.

	1	**2**
Ni-S1, Å	2.4419(3)	2.4074(4)
Ni-S2, Å	2.4157(3)	2.4109(4)
Ni-S3, Å	2.3859(3)	-
Ni-N1, Å	2.0988(9)	2.0795(12)
Ni-N2, Å	2.0659(9)	2.1016(12)
Ni-axial ACN	2.0651(10)	2.0609(13)
∠S1-Ni-S2, °	85.583(10)	89.395(14)
∠N1-Ni-S2, °	94.03(3)	89.59(3)

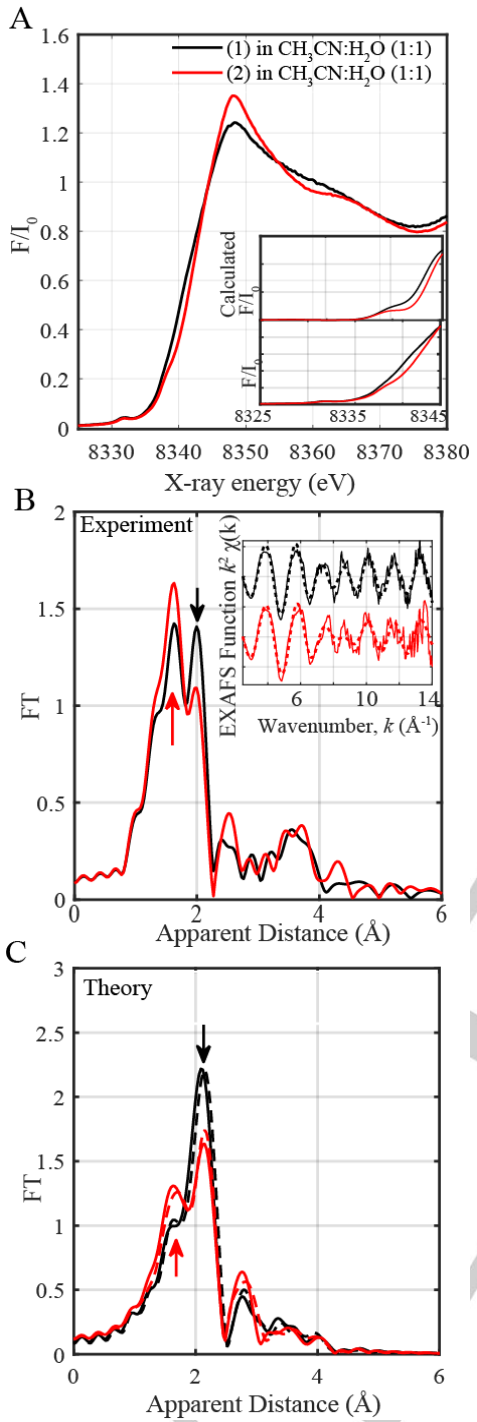

Figure 2. (A) Normalised experimental Ni K-edge XANES of catalyst **1** and **2** in 1:1 (v/v) ACN:H_2O. Inset: Details of the pre-edge and rising edge regions (Bottom Inset) in comparisons to the calculated XANES spectra (Top Inset) of catalysts **1** and **2** using DFT-optimised coordinates (B) Fourier transforms of k^2-weighted Ni EXAFS of catalyst **1** and **2** in 1:1 (v/v) ACN:H_2O. Inset: Back Fourier transforms of the experimental results (solid lines) and fitting of $k^2\chi(k)$ (dashed lines). Experimental spectra were calculated for k values of 2.486 to 14 Å^{-1}. (C) Simulated EXAFS spectra (solid lines); atomic coordinates were obtained from single crystal X-ray diffraction structure of catalyst **1** and **2** and from DFT simulations (dashed lines).

The **Ni^{II}** complexes of **1** and **2** were studied by XANES and EXAFS (Figure 2) in a mixture of acetonitrile and water. Although the metal centres in both complexes have the same oxidation states, the local coordination spheres and geometries of both complexes are clearly different explaining the shift in energy and changes in the 1s → 4p main transitions along the rising edge. The energy shift is well-reproduced by the spectra simulated by time-dependent density functional theory (TD-DFT) methods (Figure 2A inset) showing that geometry optimizations and ab-initio XANES simulations used for both catalysts reproduce the experimental data well.

The EXAFS spectra of complexes **1** and **2** are shown in Figure 2B. Two prominent peaks are observed in both spectra corresponding to the distinct Ni-N and Ni-S bond distances. Analysis of the first peak in **1** clearly resolves 3 Ni-N distances at 2.05 Å, and inclusion of 3 Ni-S distances at 2.41 Å improves the quality of the first as shown by the decreased R-factors and χ^2 values (Table S1, fits 3 and 4). The XANES and EXAFS of catalyst **1** in pure ACN and a mixture of 1:1 ACN:H_2O are identical (Figure S1) showing that the acetonitrile molecules stay bound to the **Ni^{II}** centre even in the presence of water. Similarly, fitting of **2** illustrates improvement of the fit quality with 4 Ni-N and 2 Ni-S distances at 2.06 Å and 2.40 Å, respectively. The increased Ni-N and decreased Ni-S coordination numbers in **2** are clearly demonstrated by the increased amplitude of the first peak and decrease in the second peak's intensity in comparison to complex **1**. The fitted Ni-N and Ni-S bond distances are in agreement with the reported XRD structures and relaxed structures from DFT geometry optimizations. Further changes detected in experimental EXAFS for complexes **1** and **2** correlate well with the data trends from XRD analysis and FEFF simulations of DFT-optimised coordinates (see SI) as shown in Figure 2C confirming that these methods can be reliably used for the analysis of the unknown transient species involved in the photocatalytic cycle.

Electrochemical characterization

The redox behaviours of the two complexes were also characterised by cyclic voltammetry (CV) as shown in Figure 3. **1** and **2** show a first quasi-reversible reduction peak at -0.95 V and -1.13 V (*vs* $Fc^{+/0}$), respectively, attributed to the reduction of **Ni^{II}** to **Ni^{I}**. The presence of the additional sulphur atom in the pentadentate catalyst **1** provides an additional stabilization of the low oxidation state of the Ni ion compared to **2**, as evidenced by the 180 mV anodic shift. A second irreversible reduction is observed at the cathodic peaks of -1.65 and -1.51 V (*vs* $Fc^{+/0}$) for **1** and **2**, respectively. Contrary to the anodic shift observed for the first reduction of **1** compared to **2**, a 140 mV cathodic shift is observed for the second wave. This irreversible reduction wave was attributed by Kojima and *coll.*[23] to the **Ni$^{I/0}$** couple. The irreversibility of this wave was attributed to the large structural change from an octahedral **Ni^{I}** geometry to a tetrahedral **Ni^{0}** species.

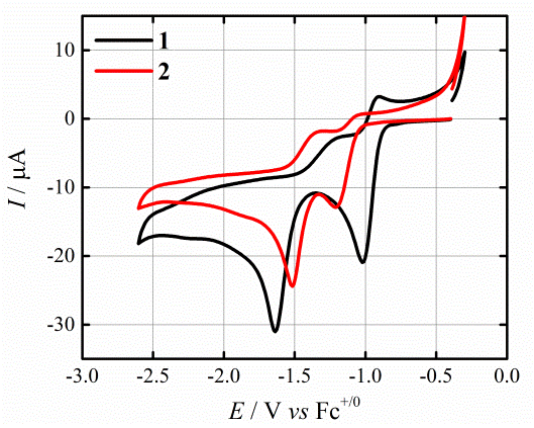

Figure 3. CVs of 1 mM catalyst **1** (black) and **2** (red) in Ar-purged ACN with 0.1 M $[Bu_4N]PF_6$, using glassy carbon as working electrode, Pt wire as counter electrode, and an $Ag/AgNO_3$ reference electrode at a scan rate of 100 mV/s.

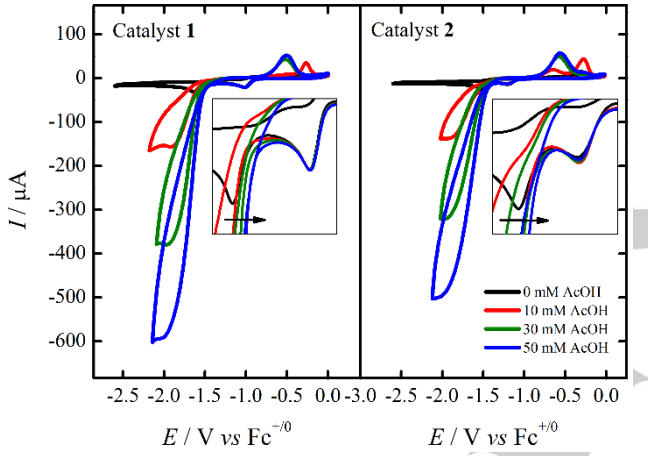

Figure 4. Effect of increasing concentrations of acetic acid (AcOH) in the CVs of 1 mM **1** (left) and **2** (right) in Ar-purged ACN with 0.1 M $[Bu_4N]PF_6$, using glassy carbon as working electrode, Pt wire as counter electrode, and an $Ag/AgNO_3$ reference electrode at a scan rate of 100 mV/s. Insets show magnified CVs at the onset potential for the catalytic reduction.

In the presence of a proton source (*i.e.* acetic acid), a catalytic current is observed at the second reduction peak of both complexes, as shown in Figure 4. Increasing the concentration of acetic acid does not shift the first reduction potential, as shown in Figure 4 inset, indicating that the reduction process for the conversion of $\mathbf{Ni^{II}}$ to $\mathbf{Ni^{I}}$ is not proton-coupled. However, in addition to the increase in the catalytic current, an anodic shift of the onset potential is observed for the second reduction wave indicating that a proton-coupled electron transfer process is involved in the catalytic H_2 evolution. In the presence of 50 mM of acetic acid, catalysts **1** and **2** show an onset catalytic potential of -1.52 V and -1.44 V (*vs* $Fc^{+/0}$), respectively. The catalytic current plateau is attained at -2.0 V (*vs* $Fc^{+/0}$) in both cases but with catalyst **1** exhibiting higher catalytic current than **2**.

After each CV measurement, it was observed that a film is adsorbed at the working electrode which required rinsing of the electrode. Roberts[24] and Dempsey[25,26] have attributed similar observation to the vulnerability of Ni-S bonds which leads to the electrochemical degradation of the catalyst in acidic media.[25] Under these conditions, the homogenous catalyst may become a precursor for a heterogeneous catalyst. This observation precluded any accurate comparative studies using electrolysis, as it would be difficult to distinguish the homogenous nature of the catalysis from the heterogeneous activity of the adsorbed film.

Photocatalytic proton reduction activity

The photocatalytic activities of catalysts **1** and **2** were investigated by coupling the catalysts with the typical $\mathbf{[Ru(bpy)_3]^{2+}}$ as a photosensitiser and ascorbate as electron donor in an optimized solvent mixture[20] containing 1:1 (v/v) dimethylacetamide (DMA) and aqueous ascorbate/ascorbic acid buffer (pH 4, 0.1 M). The solution was irradiated with a blue LED light (centred at 463 nm) to selectively excite the photosensitiser. Under these conditions, catalytic proton reduction was observed for both catalysts as evidenced by the detection of hydrogen gas by gas chromatography, as shown in Figure 5. Although catalysts **1** and **2** demonstrate lower photocatalytic activity in comparison to other Ni catalysts reported in the literature,[16,17,27,28] a clear difference in the photocatalytic activity was observed between the two complexes. Going from the tetradentate N_2S_2 ligand for catalyst **2** to the pentadentate N_2S_3 ligand for catalyst **1** improves the turnover frequency (TOF) of the photocatalytic production of H_2 from 2.2 to 3.8 h^{-1}.

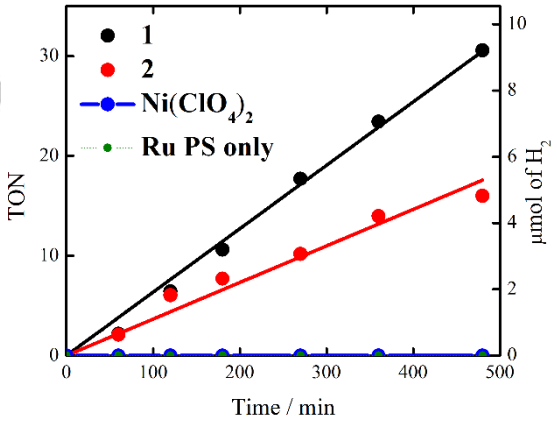

Figure 5. Photocatalytic production of H_2 gas as measured by gas chromatography of an Ar-purged 1:1 (v/v) solvent mixture of DMA and aqueous ascorbate/ascorbic acid buffer (pH 4, 0.1 M) containing 250 µM $\mathbf{[Ru(bpy)_3]^{2+}}$ with 100 µM of Ni(II) catalyst (**1** in black, **2** in red, and $Ni(ClO4)_2$ salt in blue) or without catalyst (green), under blue LED light (18 mW/cm^2).

Control experiment with $Ni(ClO_4)_2$ salt did not produce any detectable H_2 gas under the same experimental conditions indicating that any degradation to form Ni nanoparticles does not contribute to the observed catalytic activity of the catalysts. In addition, no significant changes were observed in the particle size distribution obtained by dynamic light scattering (DLS) experiments (Figure S2) of the reaction solution before and after photo-irradiation indicating the homogenous nature of the

catalysis within the milder conditions of the photocatalytic experiments. Furthermore, control experiment in the absence of the catalysts did not produce any detectable H_2 gas indicating that the observed differences in the activities are intrinsic to the catalysts, and not to trace activities of the photosensitiser.

Tracking the first photo-induced electron transfer by OTA spectroscopy

To elucidate the observed differences in the photocatalytic production of H_2, OTA spectroscopy was employed to determine the photo-induced electron transfer rates and dynamics between the photosensitiser and the catalyst. The thermodynamic potentials of each of the components of the photocatalytic system {**[Ru(bpy)$_3$]$^{2+}$** as photosensitiser denoted as **Ru^{II}**, catalysts **1** (Ni-N_2S_3) or **2** (Ni-N_2S_2), and ascorbate as the electron donor denoted as **ED**} were determined electrochemically and the energy diagram mapped in Figure 6.

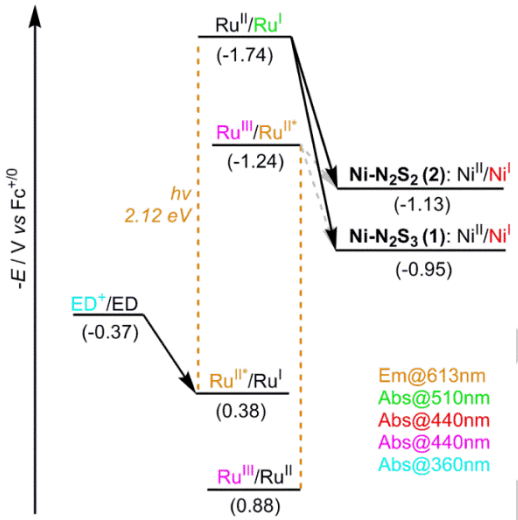

Figure 6. Thermodynamic diagram associated with the photocatalytic cycle involving the Ni catalysts **1** and **2**, Ru^{II} as photosensitiser and ascorbate as electron donor (ED). Coloured text indicates the spectral signatures monitored for the time-resolved absorption measurements.

Once the **Ru^{II}** is excited at 460 nm, a characteristic emission at 613 nm from the triplet excited state **Ru^{II}*** is observed. This excited state is efficiently quenched by ascorbate (**ED**) at a bimolecular rate constant of 2.3 x 10^8 $M^{-1}s^{-1}$ compared to the sluggish quenching by the catalyst at the same concentrations, as observed in the Stern-Volmer plots in Figure S3. This indicates that even though the excited **Ru^{II}*** is sufficiently reducing to transfer an electron to the Ni catalysts as shown by the grey dashed arrow in Figure 6, no significant oxidative quenching of the excited state of the photosensitiser by the catalyst occurs. The emission quenching by the **ED** is accompanied by a growth at 510 nm in the transient absorption spectra, indicating the formation of the one-electron reduced (OER) species of the photosensitiser, denoted as the formal **Ru^{I}** species. This is indicative of a reductive quenching mechanism where the electron is transferred from **ED** to **Ru^{II}*** forming **ED$^+$** and **Ru^{I}**.

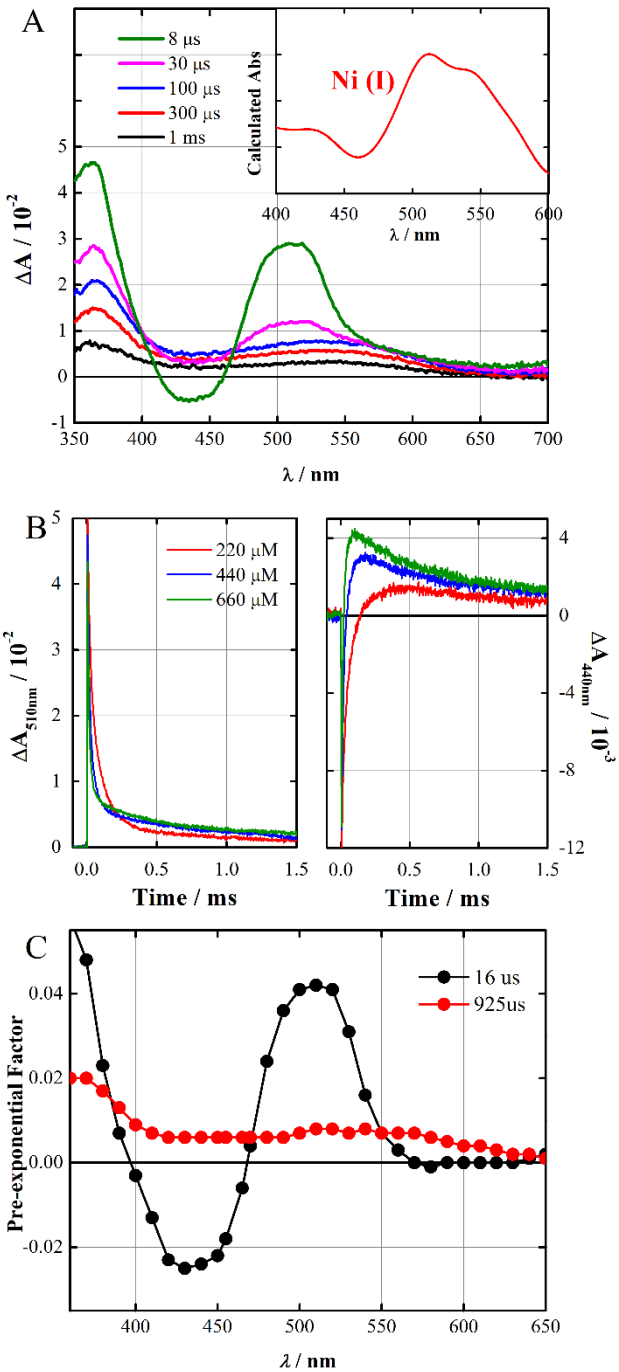

Figure 7. (A) Transient absorption spectra of 24 µM **[Ru(bpy)$_3$]$^{2+}$**, 660 µM catalyst **1**, in Ar-purged 1:1 solvent mixture of ACN and aqueous ascorbate/ascorbic acid buffer (pH 4; 0.1 M) at the indicated delay times after excitation. Laser energy = 8 mJ, λ_{exc} at 460 nm. Inset: DFT-optimised UV-Vis spectrum of **Ni^{I}** (catalyst **1**), see SI for more details. (B) Corresponding transient absorption kinetics at 510 nm (left) due to the decay of **Ru^{I}** and 440 nm (right) due to the growth of **Ni^{I}** (catalyst **1**) as a function of catalyst concentration (C) Decay associated spectra (DAS) of the transient absorption kinetics of catalyst **1** (same conditions as part A). Black lines correspond to **[(Ru^{I} + Asc^{+}) - (Ru^{II} + Asc)]** while the red lines correspond to **[(Ni^{I} + Asc^{+}) - (Ni^{II} + Asc)]**, with their respective lifetimes.

In the presence of both the **ED** and the catalyst, an absorption band at 510 nm characteristic of the **Ru^{I}** formation is first observed as shown in Figure 7A then this species decays to give rise to a new species with a characteristic positive absorption from 440 nm to 550 nm, which is assigned to the OER of catalyst **1**, denoted as **Ni^{I}**, together with an absorption band at 360 nm due to oxidised ascorbate. The optical absorption of the reduced **Ni^{I}** species was further calculated through TD-DFT for the square bipyramidal **Ni^{I}** complex without any bound solvent molecule (Figure 7A inset; comparison in Figure S6) and found to be in good agreement with the experimentally observed spectral feature of the reduced **Ni^{I}** species. Attempts to perform spectroelectrochemical measurements to determine the spectral signature of **Ni^{I}** was unsuccessful because of film deposition in the working electrode, rendering no distinguishable spectral changes in the bulk solution.

Following the kinetics at both 510 nm and 440 nm gives a clear picture that the decay of **Ru^{I}** is concomitant with the growth of **Ni^{I}**, as shown in Figure 7B. Increasing the concentration of catalyst **1** accelerates the decay of **Ru^{I}** and increases the amount of reduced **Ni^{I}** formed, due to more favourable competition of **Ni^{II}** reduction compared to charge recombination between **Ru^{I}** and oxidised ascorbate. By implementing a global fit of these kinetic data, a close-to-diffusion-limited bimolecular rate constant of 1.02 x 10^{8} $M^{-1}s^{-1}$ was determined for the electron transfer from **Ru^{I}** to **Ni^{II}** (catalyst **1**) forming **Ru^{II}** and **Ni^{I}**. Concentration-dependent transient absorption kinetics were also obtained for catalyst **2**, as shown in Figure S4. Global fitting of the kinetic data, however, yielded a rate constant of 2.48 x 10^{7} $M^{-1}s^{-1}$ for the first photo-induced electron transfer from **Ru^{I}** to **Ni^{II}** (catalyst **2**) forming **Ru^{II}** and **Ni^{I}**. This is four times slower compared to catalyst **1** (Figure 8). The difference in the thermodynamic drive (ΔG = -610 meV for **2** *vs* ΔG = -790 meV for **1**) for the first electron transfer (Figure 6) may provide a plausible explanation for this.

A global fitting procedure was employed for the transient absorption kinetics at each wavelength and resulted into two time constants, as shown in Figure 7C for catalyst **1** and Figure S5 for catalyst **2**. The first time constant (τ_1) was attributed to the concentration-dependent electron transfer from **Ru^{I}** to **Ni^{II}**. A faster time constant (τ_1 = 16 µs, Figure 7C) for catalyst **1** compared to that of catalyst **2** (τ_1 = 39 µs, Figure S5), was detected which is in accordance with the larger thermodynamic drive for **1**. The slower time constant (τ_2) was attributed to the charge recombination between **Ni^{I}** and **Asc^{+}**. The charge recombination was in fact faster for catalyst **2** (667 µs, Figure S5) compared to catalyst **1** (925 µs, Figure 7C). This difference is similarly attributed to the higher thermodynamic drive for the charge recombination between **Ni^{I}** and **Asc^{+}** for catalyst **2** (ΔG = -760 meV) compared to catalyst **1** (ΔG = -580 meV). The Decay Associated Spectra (DAS) indicate that the **Ni^{I}** species for this class of catalysts shows positive absorption from 440 nm to 550 nm in agreement with the DFT-calculated **Ni^{I}** spectrum of catalyst **1** (Figure 7A inset), and the reported chemically-reduced **Ni^{I}** spectrum of catalyst **2**.[20]

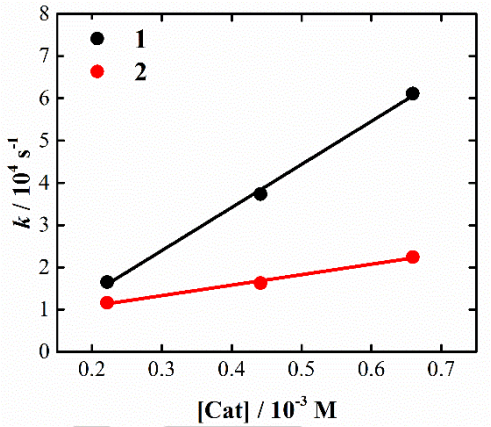

Figure 8. Comparison of the plots of globally fitted *k* against concentration of catalyst **1** (black) and catalyst **2** (red) giving electron transfer rate constants of 1.02 x 10^{8} $M^{-1}s^{-1}$ and 2.48 x 10^{7} $M^{-1}s^{-1}$, respectively.

Time-resolved XAS measurements

The kinetic information obtained through optical transient absorption analysis was used as a basis for time-resolved XAS experiments (Figure 9) in the ns-µs time range aimed at monitoring the kinetics and structural dynamics of the photo-induced **Ni^{I}** species. The more active catalyst **1** was coupled with **[Ru(bpy)$_3$]$^{2+}$** as photosensitiser in a 1:10 ratio with ascorbate as the electron donor. The complete photocatalytic system was optically pumped at 400 nm with a 10 KHz repetition-rate laser and probed with x-ray pulses at several time delays from 100 ps to 25 µs. Features in the time-resolved spectra obtained by subtracting the laser-on and laser-off (dark) spectra provided information about the transient states involved in the photocatalytic cycle. Figure 9B shows the tr-XAS spectra at an averaged delay of ~12 µs. A prominent peak at 8340 eV together with a broad dip at 8350 eV relate to the formation of the reduced **Ni^{I}** species and the bleaching of the **Ni^{II}** ground state, respectively (Figure 9B,C). These energy transitions show that the K-edge of the Ni centre shifts to lower energy, indicating the reduction of **Ni^{II}** and confirming the formation of **Ni^{I}** through one-electron transfer from the reduced **Ru^{I}**. It is important to note that no transient signal was obtained in a binary mixture of the Ni catalyst and Ru photosensitiser confirming the reductive quenching of the photosensitiser to be the predominant pathway in the photocatalytic reaction as previously confirmed through OTA spectroscopy (Figure 7).

Various geometries with different coordinated ligands for a **Ni^{I}** species were considered, namely a square bipyramidal and an octahedral geometry with a bound acetonitrile and water molecule (Figure S6). The solvent molecule is in this case loosely bound to the **Ni^{I}** metal centre with a Ni-N/O distance of ~2.91-4.30 Å. Additionally one of the Ni-S is loosely coordinated with a Ni-S bond distance of 2.56-2.77 Å. Comparison of the theoretical and experimental XANES (Figure 9B), as well as the DFT-optimised optical absorption spectra (Figure S6) with the decay associated spectra of **Ni^{I}** of catalyst **1** in Figure 7C, altogether reveal that a distorted square bipyramidal **Ni^{I}** complex with an unbound solvent molecule is the most-likely

configuration of the photo-produced **Ni^{I}** species. The sensitivity of tr-XAS experiments to the oxidation state of the metal further confirms that under these experimental conditions, a homogenous nature is still maintained due to the lack of Ni(0) transient signal that can be expected from heterogenous nanoparticle formation (Figure S7).

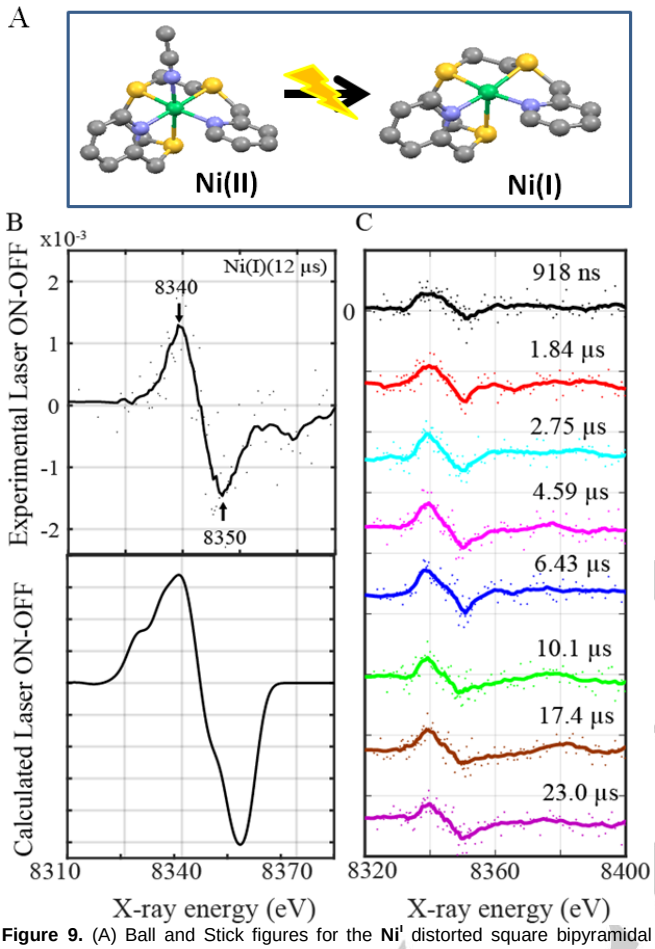

Figure 9. (A) Ball and Stick figures for the **Ni^{I}** distorted square bipyramidal geometry from catalyst **1**. (B) Top: Experimental difference spectra (Laser on-off) corresponding to the **Ni^{I}** transient signal for complex **1** at ~12 µs. Experimental condition involves an Ar-purged 1:1 solvent mixture of ACN and aqueous ascorbate/ascorbic acid buffer (pH 4; 0.1 M) containing 1 mM catalyst **1** and 10 mM **[Ru(bpy)$_3$]$^{2+}$**. Bottom: Theoretical XANES simulations corresponding to the difference between **Ni^{II}** with a bound acetonitrile molecule and **Ni^{I}** with unbound solvent molecule. (C) Stacked spectra corresponding to a series of time-delays between laser and X-ray pulses. These measurements were carried out for a range of averaged time delays from 0-23 µs for a complete photocatalytic system when purged with N_2 gas.

Proposed Photocatalytic Cycle

The elucidation of the electronic and structural configuration of the reduced **Ni^{I}** species through time-resolved XAS and DFT calculations, complemented the kinetics and spectral information obtained by optical transient absorption measurements. The comprehensive set of characterization techniques employed in this work allow us to monitor the electronic and geometric changes at the Ni centre for the **Ni-N$_2$S$_3$** catalyst (**1**) in a full photocatalytic system and suggest a plausible mechanistic pathway as illustrated in Figure 10. An acetonitrile-coordinated **Ni^{II}-N$_2$S$_3$** is initially observed when dissolved in the aqueous acetonitrile solution. Upon light excitation, the excited **Ru^{II}*** is efficiently quenched by the ascorbate electron donor producing the reduced **Ru^{I}**, which subsequently transfers an electron to the **Ni^{II}-N$_2$S$_3$** catalyst with a close-to-diffusion-limited bimolecular rate. The reduced catalytic species is a **Ni^{I}** intermediate bearing a distorted square bipyramidal geometry with an unbound solvent molecule (Figure 9A), thus undergoing a metal-centred reduction. The observed lower efficiency for the formation of the **Ni^{I}** species for **2** compared to **1** (Figure 8) is consistent with the trend observed in the photocatalytic proton reduction activities as illustrated in Figure 5.

This first photo-induced electron transfer, however, may not be the rate-determining step as hinted by the redox behaviours shown in Figure 4. Based on initial observations from cyclic voltammetry measurements, a second electron transfer is required to generate the catalytically-active species. This second electron transfer is expected to be coupled to proton transfer for the proton reduction activity. Attempts to characterise the doubly-reduced species were unfruitful. Nonetheless, based on the electrochemical characterization, it is plausible that a significant change in the coordination sphere is expected to lead to a tetragonal geometry of the formal **Ni^{0}** species. The pyridine can be expected to be knocked off the metal centre to provide a free base to dock a proton (Figure 10).[17,18,27] Protonation of this species forms a **Ni^{II}-H** that may react intramolecularly with the proton on the pyridine to form H_2 as similarly envisioned for proton-reduction catalysts bearing proton relays.[12,18,29–31] Further theoretical and experimental investigations are currently underway to confirm the nature of the **Ni** protonated and **Ni^{II}** hydride intermediates. Nevertheless, this study provides meaningful insights on the electronic and structural configuration of the photo-reduced **Ni^{I}** species involved in the protonation step and suggests plausible mechanistic pathways for the hydrogen evolution reaction pathways for this family of Ni-based catalysts.

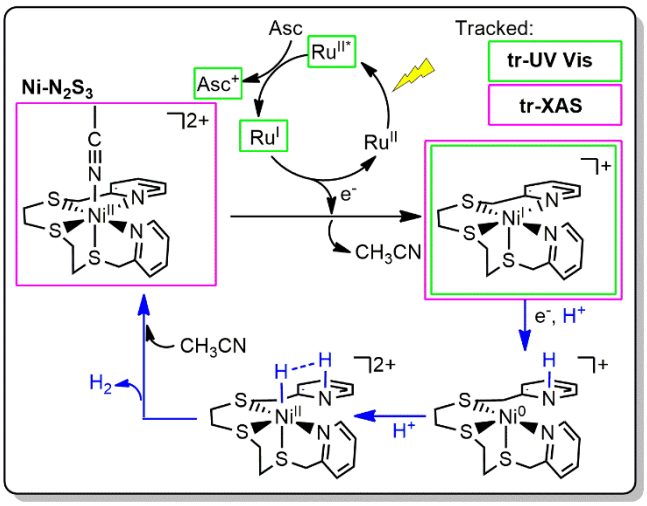

Figure 10. Proposed catalytic cycle for the photocatalytic reduction of protons by **Ni-N$_2$S$_3$** (catalyst **1**) with the coloured boxes indicating the spectroscopic tracking of the intermediates performed in this work.

Conclusions

We have found in this study that a N_2S_3 containing ligand set stabilises low oxidation states of **Ni^{I}** as observed by the 180 mV anodic shift of the **Ni$^{II/I}$** redox couple in comparison with an N_2S_2 homologue. The use of the N_2S_3 pentadentate ligand has proven to be critical for the improvement of the overall photocatalytic proton reduction activity compared to the previously reported tetradentate N_2S_2 homologue. Furthermore, the application of transient optical and time-resolved X-ray spectroscopy in combination with DFT calculations allowed us to monitor the electronic and structural dynamics of the Ni/Ru photocatalytic systems. Time-resolved analyses demonstrate the reductive quenching pathway of the excited photosensitiser to be the predominant pathway leading to a reducing **Ru^{I}** species able to transfer an electron to the Ni catalysts at a close-to-diffusion bimolecular rate. Spectroscopic studies complementarily show that the **Ni^{II}** octahedral complex is reduced to a distorted square bipyramidal **Ni^{I}** species concomitant with solvent displacement. Lastly, hints from electrochemical characterisation show that no proton is involved until the formation of the doubly-reduced Ni species required to initiate the catalytic activity. Results from this work are important to understand the charge separation dynamics in photocatalytic systems for the hydrogen evolution reaction and will be helpful to design improved catalysts for more efficient water reduction processes.

Experimental Section

Additional details on experimental techniques and characterization results can be found in the Supplementary Information (SI).

Synthesis and characterization of N_2S_3 ligand

Metallic sodium (2.48 g, 104 mmol, 4.0 eq) was reacted with absolute ethanol (150 mL) under Ar atmosphere. 2,2′-Thiodiethanethiol (3.4 mL, 26.1 mmol, 1.0 eq) was added to the solution and the mixture was heated to reflux at 85 ˚C for 30 min. Then, a solution of 2-picolyl chloride hydrochloride (8.50 g, 51.8 mmol, 2.0 eq) in absolute ethanol (100 mL) was added slowly to the reaction mixture. The mixture was stirred and refluxed at 85 ˚C for 15 h under Ar. The solvent was removed using rotary evaporator and the residue was extracted with chloroform and H_2O. The organic layer was washed with brine solution, dried over anhydrous $CaCl_2$, and filtered. The volatiles of the filtrate were evaporated using rotary evaporator and further dried under vacuum to produce brown oil of bis(2-pyridylmetyl)- 2,2′-thiodiethanethiol, denoted as **N_2S_3** (8.743 g, 25.98 mmol, 99.5% yield). ^{1}H NMR ($CDCl_3$, 298 K, 250 MHz): δ_H 2.70 (8H, s), 3.89 (4H, s), 7.20 (2H, dd), 7.39 (2H, d) 7.70 (2H, dd), 8.56 (2H, d). ESI-HRMS: calculated m/*z* = 359.0681 $[M+Na]^+$ for $C_{16}H_{20}N_2NaS_3$, found 359.0698.

Synthesis and characterization of Ni-N_2S_3 (Catalyst 1)

An equimolar solution of $Ni(ClO_4)_2$•$6H_2O$ (336 mg, 1.0 mmol, 1.0 eq) in MeOH (20 mL) was added to a solution of **N_2S_3** ligand (366 mg, 1.0 mmol, 1.0 eq) in MeOH (20 mL). The mixture was stirred for 1 hour at room temperature. The solvent was evaporated using rotary evaporator forming purplish oil. The oil was dissolved in acetonitrile and ethyl acetate was added to promote precipitation. X-ray quality crystals were grown by slow diffusion of ethyl acetate in the acetonitrile solution of the complex (438 mg, 0.69 mmol, 69% yield). ESI-HRMS: calculated m/*z* = 492.9622 $[M-(ClO_4)]^+$ for $C_{16}H_{20}N_2S_3NiClO_4$, found 492.9621.

Synthesis and characterization of N_2S_2 ligand

Metallic sodium (300 mg, 13 mmol, 4.4 eq) was reacted with absolute methanol (15 mL) under Ar. 1,2-Ethanedithiol (250 µL, 2.97 mmol, 1.0 eq) was added to the solution and stirred at room temperature. Then, the solution of 2-picolyl chloride hydrochloride (1.06 g, 6.46 mmol, 2.2 eq) in absolute methanol (7 mL) was added slowly to the mixture. The mixture was stirred for 16 h at room temperature under Ar. The solvent was removed using rotary evaporator and the residue was extracted with chloroform and H_2O. The organic layer was washed with brine solution, dried over anhydrous $MgSO_4$, and filtered. The volatiles of the filtrate were evaporated using rotary evaporator and further dried under vacuum to produce brown oil of bis(2-pyridylmetyl)-1,2-ethanedithiol, denoted as **N_2S_2** (811 mg, 2.95 mmol, 99% yield). ^{1}H NMR ($CDCl_3$, 298 K, 360 MHz): δ_H 2.70 (4H, s), 3.85 (4H, s), 7.17 (2H, dd), 7.37 (2H, d) 7.66 (2H, dd), 8.52 (2H, d). ESI-HRMS: calculated m/*z* = 299.0647 $[M+Na]^+$ for $C_{14}H_{16}N_2NaS_2$, found 299.0636.

Synthesis and characterization of Ni-N_2S_2 ligand (Catalyst 2)

An equimolar solution of $Ni(ClO_4)_2$•$6H_2O$ (392 mg, 1.0 mmol, 1.0 eq) in MeOH (10 mL) was added to a solution of **N_2S_2** ligand (292 mg, 1.0 mmol, 1.0 eq) in MeOH (10 mL). The mixture was stirred for 1 day at room temperature. The solvent was evaporated using rotary evaporator forming purplish oil. The oil was dissolved in acetonitrile and ethyl acetate was added to promote precipitation. X-ray quality crystals were grown by slow diffusion of ethyl acetate in the acetonitrile solution of the complex (376 mg, 0.61 mmol, 61% yield). ESI-HRMS: calculated m/*z* = 432.9588 $[M-(ClO_4)]^+$ for $C_{14}H_{16}N_2S_2NiClO_4$, found 432.9593.

X-ray Diffraction

X-ray diffraction data for complex **1** was collected using a Bruker AXS Kappa Apex II Diffractometer with 0.71073 Å Mo-Kα radiation. X-ray diffraction data for complex **2** was collected using a VENTURE PHOTON100 CMOS Bruker diffractometer with Micro-focus IuS source Mo Kα radiation. Crystals were mounted on a CryoLoop (Hampton Research) with Paratone-N (Hampton Research) as cryoprotectant and then flash-frozen in a nitrogen-gas stream at 100 K. The temperature of the crystal was maintained at the selected value by means of a 700 series Cryostream (for complex **1**) or N-Helix (for complex **2**) cooling device to within an accuracy of ±1 K. The data were corrected

for Lorentz polarization, and absorption effects. The structures were solved by direct methods using SHELXS-97[32] and refined against F2 by full-matrix least-squares techniques using SHELXL-2008[33] with anisotropic displacement parameters for all non-hydrogen atoms. Hydrogen atoms were located on a difference Fourier map and introduced into the calculations as a riding model with isotropic thermal parameters. All calculations were performed by using the Crystal Structure crystallographic software package WINGX.[34]

CCDC 1944952 (complex **1**) & 1944953 (complex **2**) contain the supplementary crystallographic data for this paper. These data can be obtained free of charge from the Cambridge Crystallographic Data Centre via http://www.ccdc.cam.ac.uk/Community/Requestastructure.

Optical Transient Absorption Spectroscopy

Excited state absorption characteristics were measured using an Edinburgh Instruments LP 920 laser flash photolysis spectrometer. Laser excitation pulses were generated from a Continuum Surelite Q-switched Nd:YAG laser coupled with a Continuum optical parametric oscillator (OPO) to produce an excitation pulse with 5 ns pulse duration at a wavelength of 460 nm and a typical laser energy of about 7-10 mJ per flash. The LP920 system is equipped with a 450 W Xenon arc lamp as the probe for the transient absorption measurements. Detection in the LP920 system is performed either via a Czerny-Turner blazed 500 nm monochromator (bandwidth: 1-5 nm) coupled with a Hamamatsu R928 photomultiplier tube (for kinetics mode), or via a 500 nm blazed spectrograph (bandwidth: 5 nm) coupled with a water-cooled ICCD camera Andor DH720 (for spectral mode). LP920 software was used for data acquisition, to calculate changes in optical density, for mathematical data treatment.

Time-resolved XAS measurements

Time-resolved X-ray absorption spectra were collected at 11 ID-D[35] beamlines at the Advanced Photon Source using the output from an APS standard undulator (undulator A, 3.3 cm period length and a total length of 2.4 m). The experiments were carried out using the 24 bunch timing mode of APS (in top up mode with a constant 102 mA ring current) which consists of a train of X-rays separated by 153 ns. This timing mode was suitable for this type of experiments in which the separation between two adjacent X-ray pulses are long enough for the avalanche Photodiode (APD) detectors to resolve individual X-ray pulses.

The sample was pumped at 400 nm wavelength using a regenerative amplified laser with 10 kHz repetition rate 5 ps-FWHM pulse length and laser power of 630 mW. The sample was circulated through a stainless steel nozzle into a free-flowing 550 µm cylindrical jet inside an airtight aluminium chamber, and continuously degassed with nitrogen. The X-ray and laser beam was spatially overlapped with an X-ray spot size of 100 µm(V) x 450 µm(H) and laser spot size of 170 µm(V) x 550 µm. With a liquid flow speed of around 3 m/s, the pumped laser volume was calculated to move out of the FWHM region in around 24 µs. This temporal range ensured that the excited state volume was probed more at the centre and less at the edges where the excitation fraction would be less, due to movement of the sample. Beamline 11 ID-D has an automated data digitization system which allows for all X-ray pulses after laser excitation to be collected. Such a system, together with the larger X-ray beam spot size, was very useful for our experiments, as multiple X-ray pulses after laser excitation were averaged to monitor the dynamics for the formation and decay of $\mathbf{Ni^{I}}$ transient species in the ns-µs time regime. In addition, by averaging multiple pulses, we obtained a better resolution of the main features in the pre-edge and edge regions of the transient signals.

The delay between the laser and X-ray pulses was adjusted by a programmable delay line (PDL-100A-20NS, Colby Instruments) and the X-ray fluorescence signals were collected with two APDs positioned at 90° on both sides of the liquid jet. Moreover, a combination of Z-1 filters and soller slits with conical geometry were used to reduce the background from elastically scattered X-rays. A Ni metal foil was placed between two ionization chambers downstream to the X-ray beam, and its transmission recorded with each scan for energy calibration.

Acknowledgements

This work was supported by CEA IRTELIS PhD fellowship program (for P. Gotico), LabEx CHARMMMAT, and by the French Infrastructure for Integrated Structural Biology (FRISBI) ANR-10-INSB-05-01. D.M acknowledges funding from the Severo Ochoa Excellence program (SEV-2016-0686) from the Instituto IMDEA Nanociencia. In addition, this research used resources of the Advanced Photon Source (Beamlines 9 BM-B and 11 ID-D), a U.S. DOE Office of Science User Facility operated for the DOE Office of Science by Argonne National Laboratory under Contract No. DE-AC02-06CH11357. Sector 9 BM-B operations were also supported by the Canadian Light Source and its funding partners. Dr. Maité Paternostre is also acknowledged for the DLS measurements.

Keywords: Bio-inspired Catalysts • Hydrogen • Optical Transient Absorption • Photocatalysis • Time-Resolved X-ray Absorption Spectroscopy

[1] J. C. Fontecilla-Camps, A. Volbeda, C. Cavazza, Y. Nicolet, *Chem. Rev.* **2007**, *107*, 4273–4303.
[2] W. Lubitz, H. Ogata, O. Rüdiger, E. Reijerse, *Chem. Rev.* **2014**, *114*, 4081–4148.
[3] T. R. Simmons, G. Berggren, M. Bacchi, M. Fontecave, V. Artero, *Coord. Chem. Rev.* **2014**, *270–271*, 127–150.
[4] S. Kaur-Ghumaan, M. Stein, *Dalton Trans.* **2014**, *43*, 9392–9405.
[5] V. Artero, M. Fontecave, *Coord. Chem. Rev.* **2005**, *249*, 1518–1535.
[6] D. Sellmann, J. Sutter, *Acc. Chem. Res.* **1997**, *30*, 460–469.
[7] D. Sellmann, F. Geipel, M. Moll, *Angew. Chem. Int. Ed* **2000**, *39*, 561–563.
[8] D. Sellmann, F. Geipel, F. W. Heinemann, *Chem. Eur. J.* **2002**, *8*, 958–966.
[9] C. Tard, C. J. Pickett, *Chem. Rev.* **2009**, *109*, 2245–2274.
[10] E. Bouwman, J. Reedijk, *Coord. Chem. Rev.* **2005**, *249*, 1555–1581.
[11] D. Brazzolotto, M. Gennari, N. Queyriaux, T. R. Simmons, J. Pécaut, S. Demeshko, F. Meyer, M. Orio, V. Artero, C. Duboc, *Nat. Chem.* **2016**, *8*, 1054–1060.

[12] M. L. Helm, M. P. Stewart, R. M. Bullock, M. R. DuBois, D. L. DuBois, *Science* **2011**, *333*, 863–866.
[13] B. E. Barton, T. B. Rauchfuss, *J. Am. Chem. Soc.* **2010**, *132*, 14877–14885.
[14] S. Canaguier, M. Field, Y. Oudart, J. Pécaut, M. Fontecave, V. Artero, *Chem. Commun.* **2010**, *46*, 5876–5878.
[15] K. Weber, T. Krämer, H. S. Shafaat, T. Weyhermüller, E. Bill, M. van Gastel, F. Neese, W. Lubitz, *J. Am. Chem. Soc.* **2012**, *134*, 20745–20755.
[16] M. P. McLaughlin, T. M. McCormick, R. Eisenberg, P. L. Holland, *Chem. Commun.* **2011**, *47*, 7989–7991.
[17] Z. Han, W. R. McNamara, M.-S. Eum, P. L. Holland, R. Eisenberg, *Angew. Chem. Int. Ed* **2012**, *51*, 1667–1670.
[18] Z. Han, L. Shen, W. W. Brennessel, P. L. Holland, R. Eisenberg, *J. Am. Chem. Soc.* **2013**, *135*, 14659–14669.
[19] H. Rao, Z.-Y. Wang, H.-Q. Zheng, X.-B. Wang, C.-M. Pan, Y.-T. Fan, H.-W. Hou, *Catal. Sci. Technol.* **2015**, *5*, 2332–2339.
[20] D. Hong, Y. Tsukakoshi, H. Kotani, T. Ishizuka, K. Ohkubo, Y. Shiota, K. Yoshizawa, S. Fukuzumi, T. Kojima, *Inorg. Chem.* **2018**, *57*, 7180–7190.
[21] B. Adhikary, S. Liu, C. R. Lucas, *Inorg. Chem.* **1993**, *32*, 5957–5962.
[22] S. Liu, C. R. Lucas, R. C. Hynes, J.-P. Charland, *Can. J. Chem.* **1992**, *70*, 1773–1783.
[23] D. Hong, Y. Tsukakoshi, H. Kotani, T. Ishizuka, T. Kojima, *J. Am. Chem. Soc.* **2017**, *139*, 6538–6541.
[24] M. Fang, M. H. Engelhard, Z. Zhu, M. L. Helm, J. A. S. Roberts, *ACS Catal.* **2014**, *4*, 90–98.
[25] B. D. McCarthy, C. L. Donley, J. L. Dempsey, *Chem. Sci.* **2015**, *6*, 2827–2834.
[26] D. J. Martin, B. D. McCarthy, C. L. Donley, J. L. Dempsey, *Chem. Commun.* **2015**, *51*, 5290–5293.
[27] H. Rao, W.-Q. Yu, H.-Q. Zheng, J. Bonin, Y.-T. Fan, H.-W. Hou, *J. Power Sources* **2016**, *324*, 253–260.
[28] H. Cui, J. Wang, M. Hu, C. Ma, H. Wen, X. Song, C. Chen, *Dalton Trans.* **2013**, *42*, 8684–8691.
[29] M. R. DuBois, D. L. DuBois, *Chem. Soc. Rev.* **2008**, *38*, 62–72.
[30] Y. Yang, M. Wang, L. Xue, F. Zhang, L. Chen, M. S. G. Ahlquist, L. Sun, *ChemSusChem* **2014**, *7*, 2889–2897.
[31] K. Majee, J. Patel, S. Rai, B. Das, B. Panda, S. K. Padhi, *Phys. Chem. Chem. Phys.* **2016**, *18*, 21640–21650.
[32] G. M. Sheldrick, *SHELXS 97, Program for the Solution of Crystal Structure*, University Of Göttingen, Germany, **1997**.
[33] G. M. Sheldrick, *Acta Cryst. A* **2008**, *64*, 112–122.
[34] L. J. Farrugia, *J. Appl. Crystallogr.* **1999**, *32*, 837–838.
[35] L. X. Chen, X. Zhang, *J. Phys. Chem. Lett.* **2013**, *4*, 4000–4013.

Entry for the Table of Contents (Please choose one layout)

Layout 2:

FULL PAPER

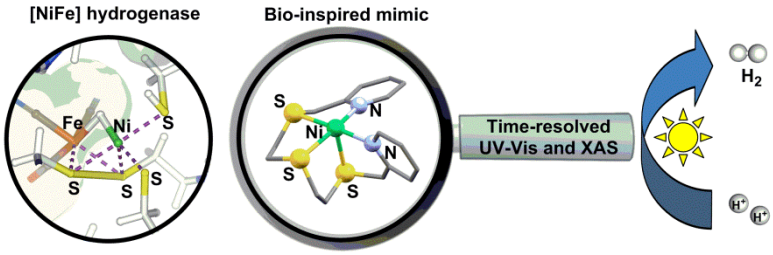

Copy that! Inspired by the sulphur-rich environment of [NiFe] hydrogenase, a novel Ni-based proton reduction catalyst bearing an acyclic pentadentate N_2S_3 ligand has been shown to improve photocatalytic activity and has been mechanistically probed by time-resolved optical and X-ray absorption spectroscopy.

Philipp Gotico, Dooshaye Moonshiram, Cunming Liu, Xiaoyi Zhang, Régis Guillot, Annamaria Quaranta, Zakaria Halime, Winfried Leibl, Ally Aukauloo**

Page No. – Page No.

Spectroscopic Characterization of Bio-inspired Ni-based Proton Reduction Catalyst Bearing Pentadentate N_2S_3 Ligand with Improved Photocatalytic Activity